nature communications

Article

https://doi.org/10.1038/s41467-025-58952-7

Large-scale 3D printed fouling-resistant self-floating evaporator

Received: 15 May 2024

Accepted: 8 April 2025

Published online: 17 April 2025

Check for updates

Yiru Pu[1,2,7], Wenzhu Lin[1,2,7], Xiaoxue Yao[1,2,7], Qili Xu[1,2,3,7], Wai Kin Lo[1,2], Yuyi Liu[1,2], Jiawei Sun[3], Yijun Zeng[1,4], Songnan Bai[5], Miaomiao Cui[4], Stevin Pramana[6], Tong Li[1,2], Zuankai Wang[4] ✉ & Steven Wang[1,2] ✉

Solar-driven interfacial desalination is an emerging approach to address global freshwater crisis while minimizing carbon emissions. A key challenge in interfacial desalination technology is maintaining long-term high efficiency with fouling-resistance and energy-saving. Here, we develop a 3D-printed concave-shaped solar evaporator and a floating freshwater collection setup, that achieve nearly 100% photothermal evaporation efficiency with a rate of 2.23 $kgm^{-2}h^{-1}$ and freshwater collection rate of 1.23 $kgm^{-2}h^{-1}$ under one sun illumination. This 3D concave-shaped solar evaporator design, achieved through 3D printing and double-sided surface modification, allows interfacial desalination process to occur at the bottom surface of the evaporator with superior heat transfer, ultra-effective salt-resistance and enlarged water-air interfacial area. The evaporation stability, extending well beyond traditional limitations of days or months, is realized by a decoupling design and the low-cost renewal of water-intake layer. This design allows vapor to escape downward without causing fouling problem within the top solar absorber. Furthermore, a self-floating freshwater collection setup facilitates thermal exchange with low-temperature seawater for sustainable application. Our large-scale integrated 3D printed evaporator-collector strategy demonstrates potential for portable solar-driven interfacial desalination and freshwater collection.

The global freshwater scarcity and severe water pollution have spurred widespread interest in developing practical methods to efficiently collect freshwater with net zero impact[1]. With approximately 71% of the Earth's surface covered by resourceful seawater, there exists substantial potential for the advancement of desalination methods[2]. Nowadays, green solar energy integrated phase change working principle ensures that solar still distillation (SSD) possesses advantages such as decentralization, cost-effectiveness, zero active energy consumption, low carbon emissions, and safety[3–6]. More efficiently, the solar evaporator initiates photothermal conversion as its initial step and confines seawater to a limited surface area for local heating and evaporation. Subsequently, the internal moisture condenses on the inner surfaces, along with the production of freshwater[7–9].

However, there come potential issues unexpectedly, such as salt scale within solar evaporators, interference between incident light and evaporated vapor, and instability caused by interaction between solar evaporator and impurities in seawater[10,11]. Many research introduced material-based solar evaporator design and system-based desalination

[1]Department of Mechanical Engineering, City University of Hong Kong, Hong Kong SAR, China. [2]Centre for Nature-Inspired Engineering, City University of Hong Kong, Hong Kong SAR, China. [3]School of Energy and Environment, City University of Hong Kong, Hong Kong SAR, China. [4]Department of Mechanical Engineering, The Hong Kong Polytechnic University, Hong Kong SAR, China. [5]Department of Biomedical Engineering, City University of Hong Kong, Hong Kong SAR, China. [6]School of Engineering, Newcastle University, Newcastle upon Tyne, UK. [7]These authors contributed equally: Yiru Pu, Wenzhu Lin, Xiaoxue Yao, Qili Xu. ✉e-mail: zk.wang@polyu.edu.hk; steven.wang@cityu.edu.hk

design to mitigate this problem. A hydrophobic material design inspired by the water lily was proposed to prevent salt buildup within the solar absorber layer, ensuring sustainable and high evaporation performance[12]. Additionally, the anti-fouling mechanism of salt self-dissolution in macro array channels and inherent microporous structures was proposed by Kuang[13]. Furthermore, a contactless structure design introduced a gap between the top solar absorber layer and the water-intake layer for salt resistance[14]. Apart from salt-fouling issue, other issues caused by water impurities and setup installation may lead to unstable evaporation performance and low-efficiency condensation. Diverging from conventional water collection systems through upward vapor condensation and collection, several researchers developed downward vapor-water conversion to avoid potential optical and thermal loss[15–18]. However, they require additional pumps to supply water or control water flowrate for evaporation, and salt residue problems within the wick or on the surface of the Janus-interface solar-steam generator (J-SSG) also require more consideration[19,20].

Recently, green energy consumption and advanced portable design have facilitated a win-win relationship between the environment and the economy[21–32]. In this work, we propose a self-floating solar desalination setup endowing the advantage of reduced carbon emissions[28], portable installations, and natural cooling resource. Meanwhile, the three-dimensional hierarchical structure design realizes both optimal solar-thermal conversion property and anticorrosion performance. This decoupling single-stage floating setup consists of several key components: a 3D concave-shaped $AlSi_{10}Mg$ composite solar evaporator, a two-dimensional (2D) water-intake layer, a bottom lattice-like resin support, and a self-floating freshwater collector (Supplementary Fig. 1). Through decoupling layers of the concave-shaped solar evaporator, vapor escapes in the downward direction without causing salt clogs within the solar absorber layer (Fig. 1a). The top solar evaporator (Fig. 1b) conducts high-efficiency solar-thermal conversion and thermal reabsorption in designed macro concave structure. The enlarged bottom surface of the solar evaporator also enhances the water-air interfacial area and evaporation performance (photothermal evaporation efficiency of nearly 100% and evaporation rate of 2.23 $kgm^{-2}h^{-1}$), endowing it a competitive candidate among recently fabricated solar evaporators (Fig. 1c). Additionally, the microstructure design as well as bilayer surface modification endows this evaporator corrosion resistance to both water and other impurities (corrosion potential of −0.59 V). The downward escaped vapor derived by vapor gradient pressure condenses on the inner wall of the collector, accompanied by thermal convection with low-temperature seawater. For freshwater collection, the self-floating setup equipped with copper fins improves condensation rate by efficient thermal transfer and enlarged vapor-water conversion area (freshwater collection rate of 1.23 $kgm^{-2}h^{-1}$).

Results

Characterization of 3D printed concave-shaped solar evaporator

The 3D concave-shaped solar evaporator is composed of three layers, as shown in Fig. 2a. From top to bottom (Fig. 2d) are polypyrrole (PPy)-decorated photothermal layer, thermal conductive 3D skeleton (Supplementary Fig. 4), and superhydrophobic anticorrosion layer. The hierarchical 3D metal alloy template fabricated by 3D printing method incorporates macro concave structures and microstructures, facilitating thermal radiation and convection reabsorption, and corrosion resistance to both water and other impurities. Aluminum alloy (A-A) as a thermal conductivity layer contributes to thermal transfer from the top surface to the bottom surface (Fig. 2f). Compared to bulk A-A, 3D printed A-A is more applicable for the following bilayer coatings due to its uniform element distribution (the structure design with varied dimensional parameters has been provided in the Supplementary Fig. 2). The presence of silicon element in A-A is also crucial to assist effective top-surface electrodeposition process, as it serves as an electronic pathway for the formation of PPy nanoparticles[33]. After surface cleaning and etching of A-A, it was soaked in a chemical solution to form an oxidized aluminum alloy (A-O) coating shown in Fig. 2c. The oxidized coating layer features volcanic-like nanoparticles and pancake-like nanoflakes (Supplementary Figs. 5 and 6), acting as a transition layer for PPy coating on the top side and an anticorrosion layer on the bottom side. The Si-O-Al compounds constructed on the surface of the oxidized aluminum alloy are also verified by EDS analysis shown in Supplementary Fig. 7, and XRD analysis evidenced by peaks at 2θ of 27.3° and 45.2° (Supplementary Fig. 8). In particular, the oxidized silicon and aluminum preferentially form Al_2SiO_5 and $NaAlSi_3O_8$ in Si-rich micro-regions, consistent with previous studies[33,34]. The sealing treatment by using melted PTFE nanoparticles at the bottom

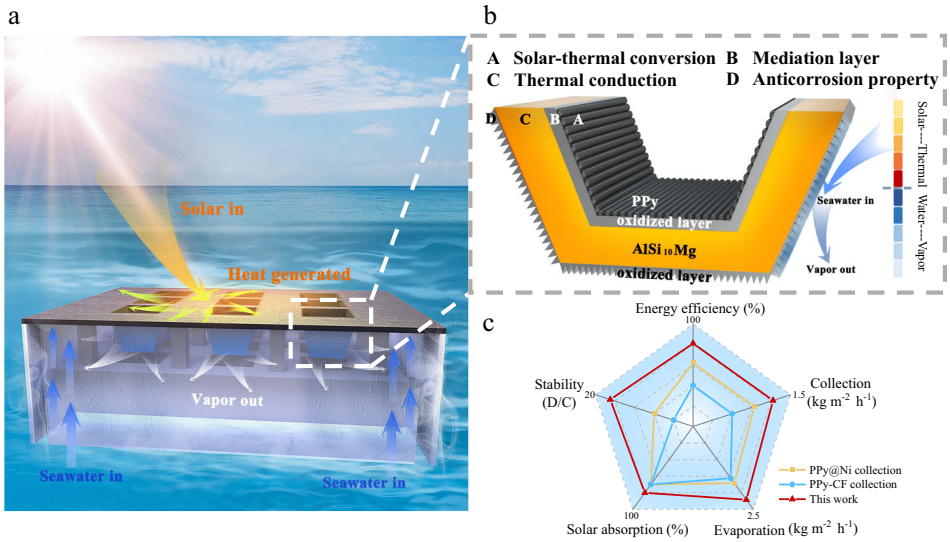

Fig. 1 | 3D hierarchical floating setup for photothermal interfacial evaporation. **a** Schematic illustration of a floating evaporation setup for downward vapor escape. **b** Schematic illustration of 3D concave-shaped solar evaporator and solar-vapor conversion (gradient-colored patterns: the blue dashed line denotes interfacial surface, and rectangular patterns denote top solar-thermal and bottom water-vapor conversion). **c** Performance comparison with other PPy-based evaporation technologies from five perspectives (Solar absorption starts at 90% and the other aspects begin at 0. Data sourced from Supplementary Table 2)[49,50].

https://doi.org/10.1038/s41467-025-58952-7

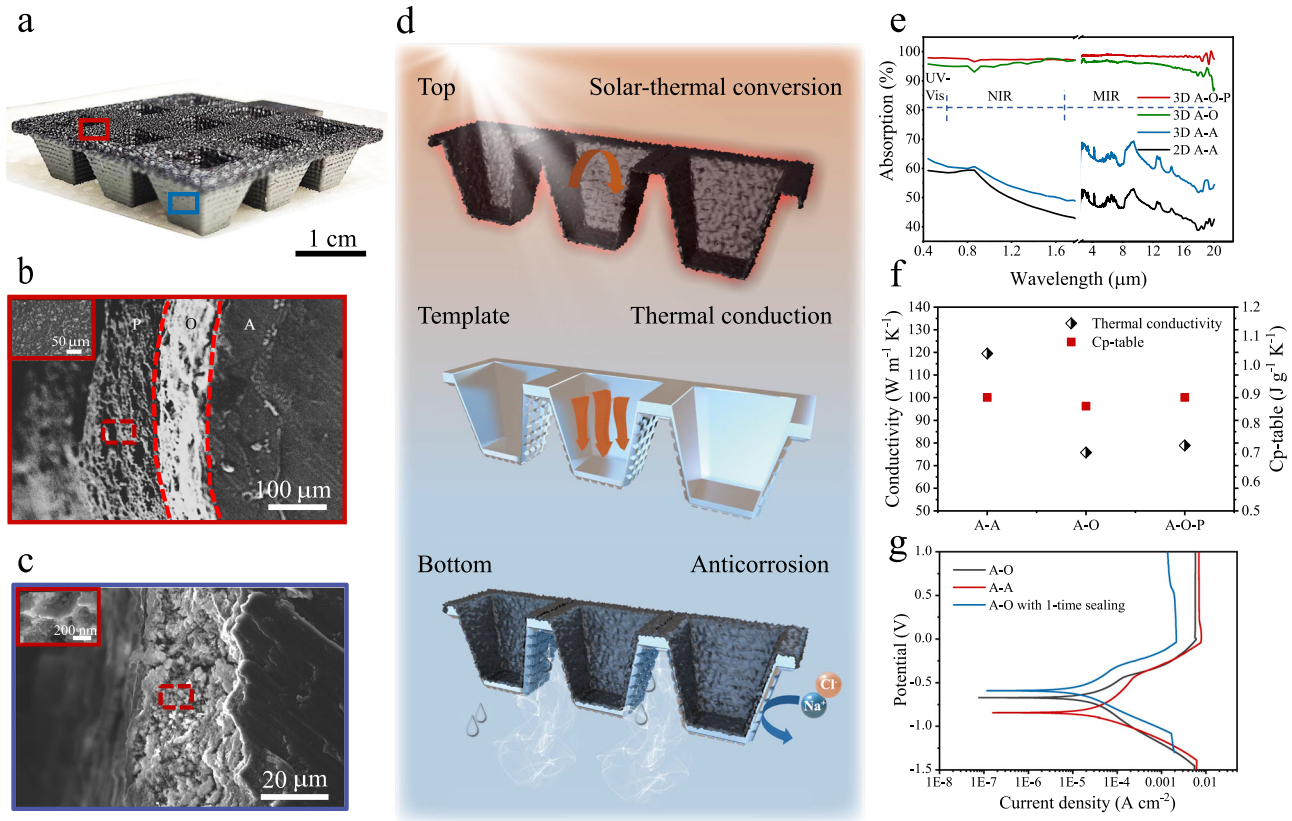

Fig. 2 | Characterization of hierarchical solar evaporator with decoupling layers and enhanced performances. a The digital picture of 3D concave-shaped solar evaporator with bilayer modifications. **b** SEM image depicting the top surface coating of A-O-P evaporator, in order from left to right are PPy nanoparticles layer (P), oxidized aluminum alloy layer (O) and aluminum alloy layer (A). The inset SEM image shows the distribution of PPy nanoparticles at high magnification, scale bar is 50 μm. **c** SEM image showing the oxidized aluminum alloy layer (A-O), featured with nanoparticles and nanoflakes (Inset SEM image shows its nanostructures, scale bar is 200 nm). **d** Schematic illustration of the components and corresponding functions of a 3D concave-shaped solar evaporator from top to bottom layers. **e** The solar absorption spectra of different specimens in UV-Vis (400 nm to 2 μm) and FTIR (2.5 μm to 20 μm) regions. **f** The thermal conductivity and Cp-table properties of A-A, A-O and A-O-P. **g** The anticorrosion performance of A-A, A-O, and A-O with one-time PTFE sealing treatment.

surface of A-O contributes to corrosion resistance (Fig. 2g and Supplementary Fig. 9), indicated by the peak at 2θ of 18.6°. Meanwhile, the A-O transition layer reduces the electrodeposition potential to a lower level, acting as a passive film for depositing PPy nanoparticles on the top surface (Supplementary Fig. 10). PPy-decorated aluminum composite (A-O-P) layer, as a top solar-thermal converter (Fig. 2b and e), was fabricated by partial surface wrapping method and electrodeposition (more details are described in the fabrication section). The EDS analysis of A-O-P demonstrates that carbon is uniformly distributed in the outer layer of the oxidized aluminum alloy, consistent with the XRD analysis exhibiting corresponding peaks at 2θ of 23.6° and 21.2°.

Photothermal effect of solar evaporator

To quantitatively characterize solar absorption capability, optical spectra of A-A, A-O, and A-O-P specimens over a wavelength range from 400 nm to 20 μm were measured (Fig. 2e and Supplementary Fig. 11). An ultraviolet–visible–near infrared (UV–vis–NIR) spectrophotometer with an integrated sphere was used to measure the absorption spectra (400 nm to 2 μm). Compared to 2D A-A with an average measured solar absorption of ~51.6%, 3D concave-shaped A-A features an average measured solar absorption of ~55.7% by the advantage of solar trapping in the concave structure. Besides, the nanostructures of the oxidized layer dampen solar reflection on nano scale with significantly enhanced solar absorption of ~96.3%. Furthermore, 3D A-O-P performs an average measured solar absorption of ~98.1% due to PPy nanoparticles decoration (Supplementary Fig. 11). To further analyze the pure thermal energy gain by considering solar energy gain and thermal loss, Fourier transform infrared spectroscopy (FTIR) in the mid-infrared range (2.5 μm to 20 μm) was utilized to collect absorption spectra of A-A, A-O, and A-O-P in both 2D and 3D dimensions. The thermal energy gain is evaluated from multiple directions incorporating solar absorption, thermal dissipated radiation, thermal convection, and thermal conduction. More specifically, pure solar energy gain is introduced to evaluate heat flux in the solar interfacial evaporation, as depicted by the following formula[35–37]:

$$P_p = P_{abs} - P_{rad} - P_{non-radiative} \quad (1)$$

where P_{abs} is the total absorbed solar power during daytime solar absorption, P_{rad} denotes radiation, and $P_{non\text{-}radiative}$ corresponds to non-radiative heat transfer including convection and conduction. The calculation methods of each thermal performance are detailed in Supplementary Note 1. As shown in Figs. S12, 3D concave-shaped A-O-P and A-O own pure energy gain of 890 W m^{-2} and 873 W m^{-2} under one sun illumination respectively, exhibiting the advantage of the PPy nanoparticles decoration and structural modifications. Each unit of 3D A-O-P features a low-temperature edged area and a high-temperature central concave region (Fig. 3a). The edged area conducts thermal convection with ambience, while the central concave region facilitates thermal convection and radiation reabsorption in cooler locations. This hierarchical temperature profile, characterized by a divergence between the edge and central areas, is evident throughout the entire

https://doi.org/10.1038/s41467-025-58952-7

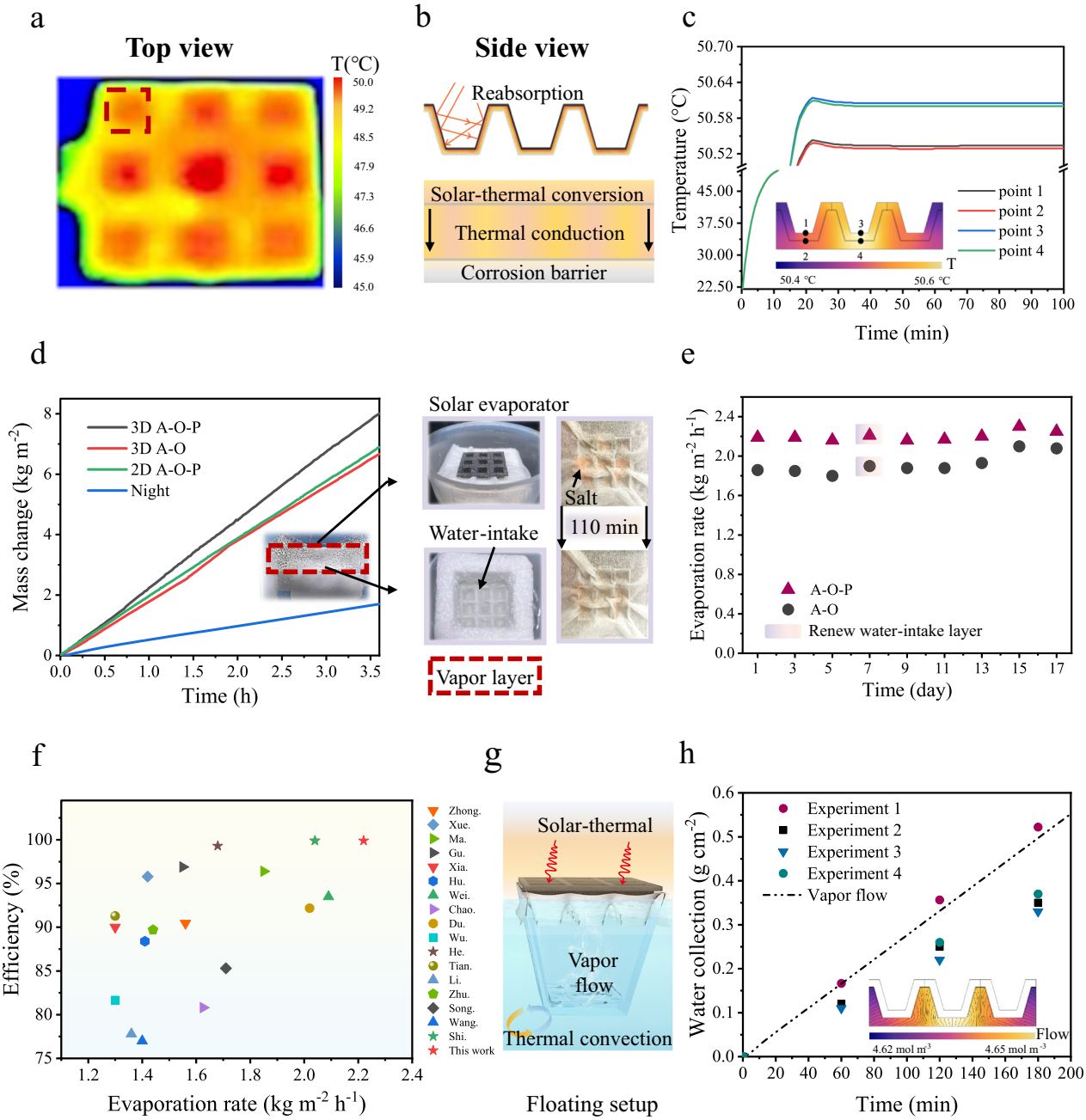

Fig. 3 | Evaporation and downward freshwater condensation of 3D hierarchical decoupling evaporator. a The top hierarchical temperature profile of the 3D concave-shaped solar evaporator, implying thermal convection reabsorption and radiation reabsorption in macro concave structure. **b** The side view of the 3D concave-shaped solar evaporator with decoupling layers. **c** The temperature simulation results at 60 min, and thermal profile (the inset image) of 3D concave-shaped solar evaporator under one sun illumination. **d** The evaporation performance of a floating evaporation setup (the setup shown in the inset image, and the vapor layer is highlighted by red dashed rectangular), and the procedure of 0.6 g pink-colored salt dissolution. **e** The recoverable and stable evaporation performance of 3D concave-shaped solar evaporator. **f** Summary of evaporation performance of state-of-the-art photothermal evaporators for desalination under one sun illumination[49–64]. **g** The schematic illustration of the floating desalination setup. **h** The correlation between multi-cycle freshwater collection and vapor flow simulation results (the inset image). The dashed line indicates the simulation results of vapor outflow.

evaporation process, as illustrated in Supplementary Fig. 13 and Supplementary Fig. 14. The side view of the concave-shaped temperature distribution (Fig. 3b) confirms efficient thermal transfer endowed by the printed template with high thermal conductivity. This efficient thermal transfer from the top surface to the bottom surface of the evaporator, detected by FLIR (Supplementary Fig. 15) and verified by simulation (Fig. 3c), provides thermal energy for the bottom-surface evaporation procedure.

Anticorrosion performance of solar evaporator

To estimate corrosion resistance of A-A and A-O in seawater, electrochemical open circuit potential (OCP) curves and Tafel plot were measured. The OCP values were recorded in 3.5 wt% NaCl solution by electrochemical workstation during 3600 s, after which Tafel plots were obtained within a stable OCP potential range from −1.5 V to +1.5 V. The reactive cell for anticorrosion testing was equipped with a Pt counter electrode and saturated calomel reference electrode. The

corrosion potential and corrosion current density of specimens could be determined by deriving the intersecting point of the tangent anodic and cathodic curves in the polarization diagram.

As shown in Fig. 2g, A-O (without sealing treatment) performs a corrosion potential of −0.67 V better than pure A-A with a corrosion potential of −0.85 V, implying that the oxidized layer acts as a stronger barrier for corrosion initiation and ion penetration. Similarly, the oxidized aluminum alloy features a corrosion current density of 1.84×10^{-5} A cm^{-2} lower to A-A with a corrosion current density of 2.94×10^{-5} A cm^{-2} correspondingly, suggesting a lower corrosion rate once the corrosion occurs. The optimized corrosion resistance of A-O is attributed to the fine grain size and removed impurities in the outer layer of the printed aluminum alloy, which prevents galvanic corrosion in NaCl solution. Besides, the oxidized layer of aluminum alloy acting as a coating barrier hinders the penetration of ions for corrosion resistance. The anticorrosion performance of A-O after PTFE sealing treatment was also evaluated (Supplementary Figs. 16 and 17), where A-O after one-time sealing treatment (in this design) shows a corrosion potential of −0.59 V and a corrosion current of 1.29×10^{-5} A cm^{-2}. It is worth mentioning that sealing treatment with melted PTFE nanoparticles could fill the holes of the oxidized layer for salt hindrance, and therefore it results in better performance than the sealing treatment with partially melted PTFE nanoparticles. The water-repellent property of the bottom surface was also evaluated by contact angle testing and droplet bouncing testing (Supplementary Figs. 18 to 21). It reveals that macro structural A-A becomes more hydrophobic with a contact angle from 115.2° to 128.5° after chemical oxidation and sealing treatment. The hierarchical A-A structure, featuring both macro concave structure and microstructures, exhibits a contact angle of 135.5°. Through chemical oxidation and sealing treatment, it undergoes a transformation into a superhydrophobic material, further enhancing its water repellence. There are in-situ snapshots of droplets, depicting that the dripped droplet bounces off from the side surface and then drops to the bottom side. The relationships between cycles of sealing treatment at the bottom side of the A-O and evaporation performance are summarized in Supplementary Fig. 25. This exploration further confirms the feasibility of our anticorrosion treatment for surface protection.

Performance of downward desalination design

The essential components of solar evaporation setup involve a 3D concave-shaped solar absorber, a 2D water-intake paper layer, and a lattice-like resin support. Compared to 2D A-O-P with an evaporation rate of 1.86 kg m^{-2} h^{-1} under one sun illumination, 3D concave-shaped A-O-P with an enlarged interfacial area and higher solar-thermal efficiency achieves an evaporation rate of 2.23 kg m^{-2} h^{-1}, calculated after subtracting evaporation rate in dark environment (Supplementary Fig. 22). The detailed calculation of evaporation efficiency is demonstrated in Supplementary Note 2. As Fig. 3d and Supplementary Fig. 23 illustrate, A-O-P with seawater evaporation rate of 2.23 kg m^{-2} h^{-1} performs better than A-O with an evaporation rate of 1.90 kg m^{-2} h^{-1}, due to their correspondingly different photothermal performances. The time-lapse vapor behavior was captured during the downward evaporation procedure (Supplementary Fig. 24), in which the porous resin with low thermal conductivity and lightweight support the upper evaporator and water-intake layer. This vapor escape is driven by a vapor pressure gradient that directs flow from the top and central side to the bottom side, as confirmed by vapor flow simulation results. In simulation, the schematic diagram of the vapor flow and the streamline of vapor are shown in Supplementary Fig. 30 and Supplementary Movie 1. The solar absorber layer absorbs sunlight and converts it into heat energy when exposed to sunlight. The water in the water-intake layer is subsequently heated to produce water vapor, which diffuses into the vapor diffusion layer under the pressure difference. In addition to conducting evaporation testing using a 3.5 wt% NaCl solution, this setup was also assessed in a real seawater environment and high-concentration brine to evaluate the effect of different salt concentrations on its evaporation performance (Supplementary Fig. 26). In the brine (25 wt% NaCl solution), the small-scale downward desalination setup exhibits stable evaporation performance (Supplementary Fig. 27), achieving an evaporation rate of 2.08 kg m^{-2} h^{-1} during 13 days. The 2D water-intake layer tightly stacked below the top solar evaporator increases the contact area for high-rate seawater supply. This setup facilitates the dissolution of 0.6 g of NaCl salt within 110 minutes through water flow exchange with low-concentration ion water, as verified in Fig. 3d (The salt weight (3.5 wt% NaCl) is determined by 8-hour sun illuminated evaporation. Additional salt dissolution procedures and anti-fouling characterizations by differing salt weights are provided through experimental results (Supplementary Fig. 28) and simulation results (Supplementary Figs. 31 and 32). The stability testing of this evaporation setup lasts for 17 days (Fig. 3e), demonstrating that the evaporation performance of this setup returns to the same high level by renewing the water paper layer after 5 days. Even after 17 days, 3D concave-shaped solar evaporator maintains an optimal evaporation performance for downward vapor escape. The stable evaporation performance is due to the decoupling design, where water is sucked only in the bottom surface of the evaporator without any inferior impacts on the top solar-thermal conversion performance. Based on our experimental observations, replacing the water-intake layer is a low-cost and effective solution to ensure sustained evaporation performance. Cohering the rational shapes with enlarged water-air interfacial area and thermal reabsorption performance, materials with superior solar-thermal conversion efficiency and anticorrosion, and assembly with downward condensation, our A-O-P solar evaporator demonstrates optimized solar evaporation yields and stable performance compared to most existing solar evaporators, as shown in Fig. 3f and Supplementary Fig. 33. Based on the positive correlation between evaporator height and evaporation efficiency, we hypothesize that increasing the height of our evaporator holds promise for further enhancing evaporation efficiency and achieving comparability with ultrahigh-efficiency 3D evaporators[38].

Traditionally, freshwater collection systems are equipped with transparent covers over the solar evaporator for upward vapor condensation and freshwater collection. However, this may lead to both optical loss and thermal loss, caused by droplet scattering on the cover and cover material with low thermal transfer. Our designed self-floating freshwater collection box (Fig. 3g and Supplementary Fig. 34) allows vapor escape oriented from the top and central side to the bottom side, and then condensation in the cooling collection box with a rate of 1.11 kg m^{-2} h^{-1} (under one sun illumination). As shown in Fig. 3h, the experimental data of collection rates in steady state exhibits a relative agreement on the simulation result pertaining to vapor flow, indicating efficient vapor-water conversion efficiency for downward freshwater condensation. This work also studied the comparison of solar-water conversion performance among previous research (Supplementary Fig. 35). The dimensional parameters designed for the self-floating property and condensation efficiency of the cooling collection box are provided in Supplementary Fig. 36.

Field trials of large-scale solar-driven interfacial desalination setup

A large-scale floating setup was designed to evaluate the performance of solar-driven interfacial desalination (Fig. 4a), which incorporates solar evaporator, water-intake layer, PTFE film, fixed cover, and copper fin-embedded collector from the top to the bottom side (Fig. 4b). The temperature analysis of the solar evaporator and seawater was recorded in Wu Kai Sha Pebbles Beach (Hong Kong) environment during one-day testing, indicating that efficient condensation performance is promised by efficient solar-thermal conversion occurred on the top

https://doi.org/10.1038/s41467-025-58952-7

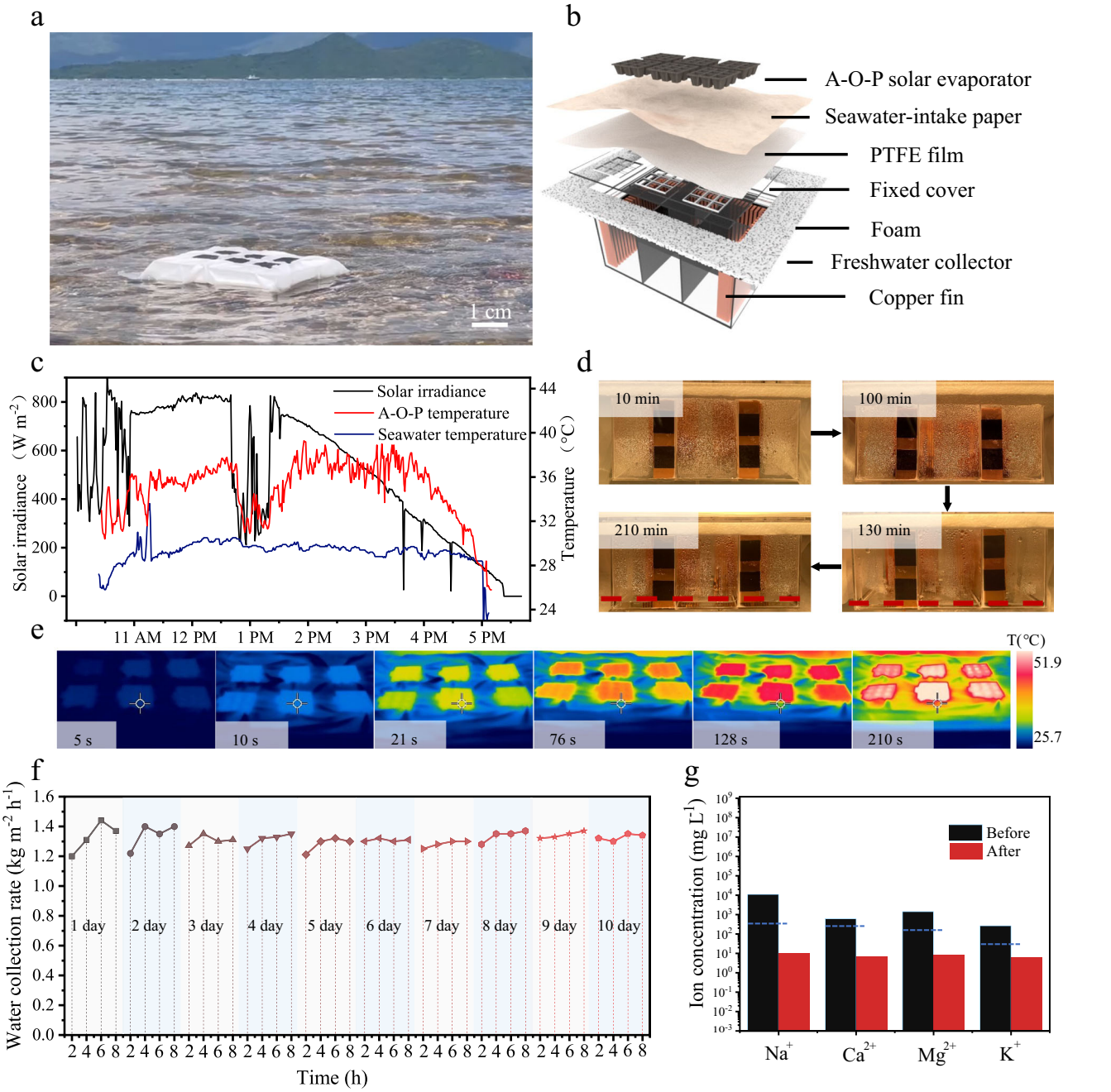

Fig. 4 | Field trials of the scale-up floating desalination setup. a The digital picture of the scale-up downward desalination setup floating on the sea at Wu Kai Sha Pebbles Beach (Hong Kong). **b** Schematic illustration of the components in the scale-up downward desalination setup. (The dimensional parameters of the collector are 24 cm × 18 cm × 9 cm (length × width × height)). **c** The real-time temperature of the 3D concave-shaped solar evaporator and synchronized outdoor environment characterization. **d** The time-lapse characterization of the vapor condensation and freshwater collection procedure. **e** The time-lapse thermal distribution in freshwater collection procedure. **f** The 10-day freshwater collection performance of the scale-up downward desalination setup. **g** The ion concentration variation in real seawater before and after desalination. The dashed blue lines indicate the WHO standard of drinking water.

evaporator and thermal convection with low-temperature seawater at the bottom side (Fig. 4c and Supplementary Fig. 38). The copper fins feature high thermal conductivity and enlarged surface area behaving as an excellent heat diffuser and thermal exchanger, enhancing the freshwater collection rate of 1.23 kg m^{-2} h^{-1}. The additional copper fins designed for large-scale application provide more sites for vapor-water conversion, performing even superior to the single module (Fig. 4d). To avoid drippage of impurities carried from the evaporation process, we added PTFE film at the bottom surface to promise the purity of the collected freshwater. The stable photothermal effect and cooling effect could also be verified by indoor FLIR testing shown in Fig. 4e and Supplementary Fig. 37. The floating seawater as a cooling resource for condensation conducts stable thermal convection during a 10-day freshwater collection period, along with zero energy consumption (Fig. 4f). In the indoor experiments, we simulated the real cooling seawater environment by exchanging the seawater constantly. The purification effect of the desalination setup was also explored by inductively coupled plasma optical emission spectroscopy (ICP-OES) to monitor ion concentrations. The variation of ion concentrations in real seawater before and after purification was recorded, where Na^+, K^+,

Ca^{2+}, and Mg^{2+} have been reduced from 10800 mg L^{-1}, 413 mg L^{-1}, 1290 mg L^{-1}, 400 mg L^{-1} to 5.0 mg L^{-1}, 0.7 mg L^{-1}, 0.8 mg L^{-1}, 0.6 mg L^{-1}, correspondingly. It is found that the concentrations of primary ions in seawater (Na^+, K^+, Ca^{2+}, and Mg^{2+}) have met the World Health Organization (WHO) standard for drinking water (Fig. 4g). In general, this large-scale 3D freshwater collection setup showcases immense potential for real-world applications.

Discussion

In summary, we have designed a 3D hierarchical solar evaporator and floating setup for interfacial evaporation and freshwater collection, incorporating 3D concave-shaped solar evaporator, 2D water-intake layer, bottom lattice-like resin support and floating freshwater collector. Combining 3D metal printing with bilayer modifications, the hierarchical solar evaporator performs high-efficiency evaporation and anticorrosion. 3D printed A-A features high thermal conductivity and uniform element distribution, performing advantages for thermal transfer and surface modifications. The designed macro concave structure and microstructure of the specimens facilitate solar trapping and thermal reabsorption. Additionally, its concave-shaped bottom surface enlarges the water-air interfacial area for water-vapor conversion in macro scale, facilitating vapor escape downward without any inferior effects on the top solar evaporator. For freshwater collection, this self-floating collection setup contributes to constant thermal convection in the cooling seawater for high-efficiency condensation, meanwhile, it exhibits more flexible and portable characteristics for non-stationary applications. The copper fins embedded in the collector also improve collection efficiency by enlarging the vapor-water conversion area. We expect this self-floating freshwater setup, together with the hierarchical solar evaporator design, will inspire broad-range explorations for sustainable development.

Methods

Design of solar evaporation/collection setup

The floating solar desalination setup from top to bottom includes 3D A-O-P solar evaporator, 2D water-intake layer carried by commercial water paper, lattice-like resin support, and freshwater collector. A 2D solar evaporator was designed as a reference group for characterization. The decoupling design in this work indicates that vapor escapes in the downward direction without causing deficient solar-thermal conversion on the top side, where the 3D concave-shaped structure design and bilayer coating of the solar evaporator ensures excellent thermal transfer and anticorrosion performance. The water-intake layer in 2D form reduces thermal loss into the bulk water, besides, it could be modified as a corresponding concave shape for high-rate water supply. A lattice-like resin support (RS-C2-GPGR-05) with thermal insulation property (thermal conductivity ~0.2 W m^{-1} K^{-1}) was fabricated by additive manufacturing. The scale-up self-floating freshwater collector incorporates fixed cover, foam, and copper fins.

Fabrication method of A-O and A-O-P

$AlSi_{10}Mg$ alloy (A-A) was printed by a 3D metal printer under 370 W at a rate of 1300 mm s^{-1}. Firstly, it was rinsed in 95% acetone solution for 15 minutes and then in isopropyl alcohol (>99.5% IPA) solution for 1 min to remove impurities on the surface. After that, the dried specimen was soaked in HCl (2 mol L^{-1}, ACS) for 10 mins to dissolve the oxidized film and then in 10 wt% NaOH (GR) to neutralize it. Then it was immersed in a chemical solution for chemical oxidation treatment, incorporating $NaCO_3$ (45 g L^{-1}, AR), NaOH (16 g L^{-1}, GR) and $NaPO_4$ (8 g L^{-1}, AR) at 65 °C for 7 mins[34,39–41]. Before electrodepositing PPy nanoparticles on the top surface of oxidized aluminum alloy, we applied partial surface sealing method by firstly melting wax at 70 °C to wrap the bottom surface of the A-O, followed by solidifying wax at room temperature. After that, 0.1 M pyrrole (CP) and 0.3 M oxalic acid (AR) were mixed at zero temperature for preparation of electrodeposition[42,43]. By controlling a voltage of 1.2 V and current of 0.03 A in electrode system, PPy nanoparticles were successfully polymerized with uniform distribution. In the electrode cell system, the specimen as the anode and the platinum plate as the counter electrode were prepared[43]. To enhance anticorrosion performance of the specimen, the bottom surface of specimen was then sealed by 15% PTFE in IPA solution[24,41,44]. Once attaining temperature at 350 °C, melted PTFE merged into the oxidized layer to form a surface barrier (the fabrication diagram is demonstrated in Supplementary Fig. 3).

Characterization

The structure of specimens was characterized by scanning electron microscopy (SEM, Sigma 500), and the composition of the specimen was analyzed by energy dispersive X-ray spectrometry (EDX, Shimadzu EDX-720) along with D2 PHASER XE-T X-ray Diffractometer System (XRD). Solar spectrum absorption measurements of the absorbers were carried out using different optical measurement systems. Hitachi UH4150 UV-Vis-NIR Spectrophotometer (attached with an integrating sphere (ISR-3100)) was used for hemispherical reflectance measurements within the UV-Vis-NIR range (400 nm to 2μm). FTIR (VERTEX 70 v) MID-IR equipped with INTEGRATIR (660-10740000) was used for reflectance measurements in mid-infrared regime (2.5 μm to 20 μm). The thermal conductivity of specimens with an average measured value was attained by Hot Disk TPS 25005. A solar simulator (CEL-PE300L-3 PerkinElmer300W) was used as an illuminant for all indoor experiments of solar desalination. During these experiments, the indoor temperature and humidity were controlled at 28 °C and ~25%, respectively. The mass change of water for calculating evaporation efficiency was measured by electronic balance and recorded by computer. The temperature profile of the specimen was captured by FLIR E8xt (incl.) and the temperature distribution of the specimen covering concave-shaped structure and edged area was measured by KEYSIGHT DAQ970A Data Acquisition System. A corrosion test in 3.5 wt% NaCl solution was prepared in a three-electrolytic cell system with Pt counter electrode as counter electrode, specimen as working electrode and saturated calomel electrode (SCE) as reference electrode[41,45]. Open circuit potential (OCP) curves and Tafel plot were measured by electrochemical station in succession. Contact angle images and time-series images were recorded by DataPhysics Contact Angle Tester and high-speed camera (pc0.dimax HS4) equipped with a zoomed lens, respectively. The outdoor atmosphere was detected by Data Acquisition Instrument (YGY-CJY4) with DC9-30V supply, equipped with thermal couples, solar intensity detector, humidity detector and wind speed detector.

Simulation details

The simulations based on the finite element method were performed using COMSOL Multiphysics version 5.6 to investigate the temperature, concentration, and velocity distribution of water vapor evaporation process under one sun illumination. A 2D component was constructed for simulation, and the geometric parameters of the model are supplied in Supplementary Fig. 29. Free triangular elements are used in meshing the model. The relative tolerance in the steady-state solver was set to 0.01[46–48]. The water evaporation process of the whole system is simulated by solving the Eqs. 2 and 3:

$$\frac{\partial c_v}{\partial t} - D\nabla^2 c_v + u \cdot \nabla c_v = R_v \tag{2}$$

$$c_v = \varphi c_{sat} \tag{3}$$

where c_v is the concentration of water vapor, D is the diffusion coefficient of water vapor, u is the velocity fields derived from the vapor diffusion, c_{sat} is the saturation concentration, φ is the relative humidity, and R_v is the rate of steam generation which is determined by the

saturation concentration c_{sat} and water activity a_w (shown as Eq. 4).

$$R_v = K(a_w c_{sat} - c_v) \tag{4}$$

where K is the evaporation coefficient ($1 \times 10^5 s^{-1}$). The heat transfer process is simulated by solving energy conversion Eq. 5:

$$\rho C_p \frac{\partial T}{\partial t} + \rho C_p u \nabla \mathrm{T} - k\nabla^2 T = Q_v \tag{5}$$

where T is temperature, ρ is the density of the fluids which are liquid water and water vapor, C_p is the heat capacity and k is the thermal conductivity. Since the evaporation is an endothermic process, the heat source Q_v in vaporization is described by Eq. 6:

$$Q_v = -H_v M_w R_v \tag{6}$$

where H_v is the latent heat of water evaporation and M_w is the molecular weight of water. Another heat source is set at the boundaries of solid surfaces to represent the heat from illumination. Meanwhile, the heat loss from natural convection and radiation on the surface of the solid is also considered. The environment temperature is set as 293.15 K. The detailed material properties and parameters that have been applied in the simulation are listed in Supplementary Table 1.

Data availability

All data supporting the findings of this study are available within the article and its supplementary files. Any additional requests for information can be directed to, and will be fulfilled by, the corresponding author(s). Source data are provided with this paper.

References

1. Mekonnen, M. M. & Hoekstra, A. Y. Four billion people facing severe water scarcity. *Sci. Adv.* **2**, e1500323 (2016).
2. Chen, C., Jiang, Y., Ye, Z., Yang, Y. & Hou, L. Sustainably integrating desalination with solar power to overcome future freshwater scarcity in China. *Glob. Energy Interconnect.* **2**, 98–113 (2019).
3. Ghaffour, N., Missimer, T. M. & Amy, G. L. Technical review and evaluation of the economics of water desalination: Current and future challenges for better water supply sustainability. *Desalination* **309**, 197–207 (2013).
4. Karagiannis, I. C. & Soldatos, P. G. Water desalination cost literature: review and assessment. *Desalination* **223**, 448–456 (2008).
5. Nandakumar, D. K. et al. Solar Energy Triggered Clean Water Harvesting from Humid Air Existing above Sea Surface Enabled by a Hydrogel with Ultrahigh Hygroscopicity. *Adv. Mater.* **31**, e1806730 (2019).
6. Chiavazzo, E., Morciano, M., Viglino, F., Fasano, M. & Asinari, P. Passive solar high-yield seawater desalination by modular and low-cost distillation. *Nat. Sustainability* **1**, 763–772 (2018).
7. Xia, Y. et al. Rational designs of interfacial-heating solar-thermal desalination devices: recent progress and remaining challenges. *J. Mater. Chem. A* **9**, 6612–6633 (2021).
8. Liu, H., Huang, Z., Liu, K., Hu, X. & Zhou, J. Interfacial Solar-to-Heat Conversion for Desalination. *Adv. energy Mater.* **9**, 1900310 (2019).
9. Cao, S. et al. Advances in solar evaporator materials for freshwater generation. *J. Mater. Chem. A* **7**, 24092–24123 (2019).
10. Wang, Z. et al. Pathways and challenges for efficient solar-thermal desalination. *Sci. Adv.* **5**, eaax0763 (2019).
11. Do Thi, H. T., Pasztor, T., Fozer, D., Manenti, F. & Toth, A. J. Comparison of Desalination Technologies Using Renewable Energy Sources with Life Cycle, PESTLE, and Multi-Criteria Decision Analyses. *Water.* **13**, 3023 (2021).
12. Xu N. et al. A water lily–inspired hierarchical design for stable and efficient solar evaporation of high-salinity brine. *Sci. Adv.* **5**, eaaw7013 (2019).
13. Kuang, Y. et al. A High-Performance Self-Regenerating Solar Evaporator for Continuous Water Desalination. *Adv. Mater.* **31**, 1900498 (2019).
14. Cooper, T. A. et al. Contactless steam generation and superheating under one sun illumination. *Nat. Commun.* **9**, 5086 (2018).
15. Jani, H. K. & Modi, K. V. Experimental performance evaluation of single basin dual slope solar still with circular and square cross-sectional hollow fins. *Sol. Energy* **179**, 186–194 (2019).
16. Velmurugan, V., Gopalakrishnan, M., Raghu, R. & Srithar, K. Single basin solar still with fin for enhancing productivity. *Energy Convers. Manag.* **49**, 2602–2608 (2008).
17. Kabeel, A. E. Performance of solar still with a concave wick evaporation surface. *Energy* **34**, 1504–1509 (2009).
18. Yadav, A. et al. Water desalination system using solar heat: A review. *Renew. Sustain. Energy Rev.* **67**, 1308–1330 (2017).
19. Wang, W. et al. Simultaneous production of fresh water and electricity via multistage solar photovoltaic membrane distillation. *Nat. Commun.* **10**, 3012 (2019).
20. Yao, H. et al. Janus-interface engineering boosting solar steam towards high-efficiency water collection. *Energy Environ. Sci.* **14**, 5330–5338 (2021).
21. Qiu, S., Li, W., Zheng, W., Zhao, H. & Wang, L. Synergistic Effect of Polypyrrole-Intercalated Graphene for Enhanced Corrosion Protection of Aqueous Coating in 3.5% NaCl Solution. *ACS Appl. Mater. interfaces* **9**, 34294–34304 (2017).
22. Roy, S. et al. Synthesis of Conducting Polypyrrole-Titanium Oxide Nanocomposite: Study of Structural, Optical and Electrical Properties. *J. Inorg. Organomet. Polym. Mater.* **27**, 257–263 (2017).
23. Canobre, S. C., Xavier, F. F. S., Fagundes, W. S., de Freitas, A. C. & Amaral, F. A. Performance of the Chemical and Electrochemical Composites of PPy/CNT as Electrodes in Type I Supercapacitors. *J. Nanomaterials* **2015**, 560164 (2015).
24. Shulga, Y. M., Vasilets, V. N., Kiryukhin, D. P., Voylov, D. N. & Sokolov, A. P. Polymer composites prepared by low-temperature post-irradiation polymerization of C2F4 in the presence of graphene-like material: synthesis and characterization. *RSC Adv.* **5**, 9865–9874 (2015).
25. Shul'ga, Y. et al. Characterisation and electrical conductivity of polytetraluoroethylene/graphite nanoplatelets composite ilms. *Appl. Phys. A* **125**, 8 (2019).
26. Si, J., Ma, R., Wu, Y., Dong, Y. & Yao, K. Microstructure and magnetic properties of novel powder cores composed of iron-based amorphous alloy and PTFE. *J. Mater. Sci.* **57**, 1–13 (2022).
27. Xu, W. et al. Flexible and Salt Resistant Janus Absorbers by Electrospinning for Stable and Efficient Solar Desalination. *Adv. Energy Mater.* **8**, 1702884 (2018).
28. Ni, G. et al. A salt-rejecting floating solar still for low-cost desalination. *Energy Environ. Sci.* **11**, 1510–1519 (2018).
29. Wang, X., Liu, Q., Wu, S., Xu, B. & Xu, H. Multilayer Polypyrrole Nanosheets with Self-Organized Surface Structures for Flexible and Efficient Solar–Thermal Energy Conversion. *Adv. Mater.* **31**, 1807716 (2019).
30. Hong, S. et al. Nature-Inspired, 3D Origami Solar Steam Generator toward Near Full Utilization of Solar Energy. *ACS Appl. Mater. Interfaces* **10**, 28517–28524 (2018).
31. Li, W., Li, Z., Bertelsmann, K. & Fan, D. E. Portable Low-Pressure Solar Steaming-Collection Unisystem with Polypyrrole Origamis. *Adv. Mater.* **31**, 1900720 (2019).
32. Li, X. et al. Three-dimensional artificial transpiration for efficient solar waste-water treatment. *Natl Sci. Rev.* **5**, 70–77 (2017).

33. Rogov, A. B., Lyu, H., Matthews, A. & Yerokhin, A. AC plasma electrolytic oxidation of additively manufactured and cast AlSi12 alloys. *Surf. Coat. Technol.* **399**, 126116 (2020).
34. Guo, Y. et al. Growth characteristics and properties of micro-arc oxidation coatings on AlSi10Mg selective laser-melted components. *Surf. Coat. Technol.* **426**, 127765 (2021).
35. Sun, X., Sun, Y., Zhou, Z., Alam, M. A. & Bermel, P. Radiative sky cooling: fundamental physics, materials, structures, and applications. *Nanophotonics* **6**, 997–1015 (2017).
36. Zhou, L. et al. Self-assembly of highly efficient, broadband plasmonic absorbers for solar steam generation. *Sci. Adv.* **2**, e1501227 (2016).
37. Zhao, H., Sun, Q., Zhou, J., Deng, X. & Cui, J. Switchable Cavitation in Silicone Coatings for Energy-Saving Cooling and Heating. *Adv. Mater.* **32**, 2000870 (2020).
38. Zhang, C. et al. Designing a next generation solar crystallizer for real seawater brine treatment with zero liquid discharge. *Nat. Commun.* **12**, 998 (2021).
39. Li, B., Wang, Y. & Gao, B. Extraction of Al from Coarse Al–Si Alloy by The Selective Liquation Method. *Materials* **14**, 3680 (2021).
40. Pezzato, L., Dabalà, M., Gross, S. & Brunelli, K. Effect of microstructure and porosity of AlSi10Mg alloy produced by selective laser melting on the corrosion properties of plasma electrolytic oxidation coatings. *Surf. Coat. Technol.* **404**, 126477 (2020).
41. Liu, C. et al. Significance of plasma electrolytic oxidation treatment on corrosion and sliding wear performances of selective laser melted AlSi10Mg alloy. *Mater. Charact.* **181**, 111479 (2021).
42. Hülser, P. & Beck, F. Electrodeposition of polypyrrole layers on aluminium from aqueous electrolytes. *J. Appl. Electrochem.* **20**, 596–605 (1990).
43. Arenas, M. A., Bajos, L. G., de Damborenea, J. J. & Ocón, P. Synthesis and electrochemical evaluation of polypyrrole coatings electrodeposited onto AA-2024 alloy. *Prog. Org. Coat.* **62**, 79–86 (2008).
44. Egorkin, V. S. et al. Atmospheric and Marine Corrosion of PEO and Composite Coatings Obtained on Al-Cu-Mg Aluminum Alloy. *Materials* **13**, 2739 (2020).
45. Egorkin, V. S. et al. Increasing thickness and protective properties of PEO-coatings on aluminum alloy. *Surf. Coat. Technol.* **334**, 29–42 (2018).
46. Eckert, E. R. & Drake, R. M. Jr. Analysis of heat and mass transfer. (1987).
47. Cussler E. L. *Diffusion: mass transfer in fluid systems*. (Cambridge university press, 2009).
48. Bergman, T. L., Lavine, A. S., Incropera, F. P. & DeWitt, D. P. *Introduction to heat transfer*. (John Wiley & Sons, 2011).
49. Zhong, X. et al. Turnover polypyrrole decorated cotton fabric based solar evaporator for cost-effective and steady desalination. *J. Clean. Prod.* **417**, 138088 (2023).
50. Song, R. et al. A self-floating Janus PPy@Ni sponge salt-resisting solar evaporator for efficient interfacial evaporation. *Appl. Surf. Sci.* **616**, 156448 (2023).
51. Xue, T. et al. Portable solar interfacial evaporator based on polyimide nanofiber aerogel for efficient desalination. *Chem. Eng. J.* **461**, 141909 (2023).
52. Ma, H. et al. A Lotus Seedpods-Inspired Interfacial Solar Steam Generator with Outstanding Salt Tolerance and Mechanical Properties for Efficient and Stable Seawater Desalination. *Small* **19**, 2304877 (2023).
53. Xia, Q. et al. A Floating Integrated Solar Micro-Evaporator for Self-Cleaning Desalination and Organic Degradation. *Adv. Funct. Mater.* **33**, 2214769 (2023).
54. Hu, Z., Ren, L., Zhang, Q. & Xiao, X. Designing Janus ZrC@fabric-based evaporator through weaving craft for stable solar interfacial desalination. *Mater. Lett.* **333**, 133619 (2023).
55. Du, Y. et al. Nature-Inspired Structure-Engineered TiN/TiO2 Nanotubes Array Toward Solar Desalination Synergy with Photothermal-Enhanced Degradation and Thermoelectric Generation. *Adv. Funct. Mater.* **34**, 2309830 (2024).
56. Chao, J. et al. Metal–Organic Framework-Derived Carbon Materials Loading on Polydopamine-Modified Polyurethane Foam for Interfacial Solar Steam Generation and Seawater Desalination. *Energy Technol.* **11**, 2201502 (2023).
57. He, J. et al. A 3D Corncob-based interfacial solar evaporator enhanced by environment energy with salt-rejecting and anti-corrosion for seawater distillation. *Sol. Energy* **252**, 39–49 (2023).
58. Tian, Y. et al. Breath-Figure Self-Assembled Low-Cost Janus Fabrics for Highly Efficient and Stable Solar Desalination. *Adv. Funct. Mater.* **32**, 2113258 (2022).
59. Li, X. et al. A 3D porous PDMS sponge embedded with carbon nanoparticles for solar driven interfacial evaporation. *Sep. Purif. Technol.* **292**, 120985 (2022).
60. Wu, W. et al. A solar-driven interfacial evaporator for seawater desalination based on mussel-inspired superhydrophobic composite coating. *Carbon* **217**, 118593 (2024).
61. Zhu, Y. et al. Low-Cost, Unsinkable, and Highly Efficient Solar Evaporators Based on Coating MWCNTs on Nonwovens with Unidirectional Water-Transfer. *Adv. Sci.* **8**, 2101727 (2021).
62. Gu, Y. et al. Facile Preparation of Cu2S/Cu Mesh For High-performance Solar Water Evaporation. *ChemistrySelect* **6**, 7901–7905 (2021).
63. Wang, Y. et al. Quasi-waffle solar distiller for durable desalination of seawater. *Sci. Adv.* **10**, eadk1113 (2024).
64. Shi, Y. et al. A 3D Photothermal Structure toward Improved Energy Efficiency in Solar Steam Generation. *Joule* **2**, 1171–1186 (2018).

Acknowledgements

This research work was funded by the General Research Fund (GRF 11217523) of Research Grant Council (RGC).

Author contributions

Y.R.P. and X.X.Y. conceived the idea. Y.R.P., X.X.Y., and W.Z.L. designed the research. Y.R.P. and Y.J.Z. performed the solar absorption experiment. Y.R.P. and J.W.S. performed the UV testing. Y.R.P. and S.N.B. performed the 3D printing experiments. Y.R.P. performed other experiments. Q.L.X. performed theoretical simulations and analyses. Y.R.P., W.Z.L., X.X.Y., Z.K.W., and S.W. analyzed the data and wrote the manuscript. W.K.L., Y.Y.L., M.M.C., S.P., and T.L. polished the manuscript. All authors contributed to discussions on the data and commented on the manuscript.

Competing interests

The authors declare no competing interests.

Additional information

Supplementary information The online version contains supplementary material available at https://doi.org/10.1038/s41467-025-58952-7.

Correspondence and requests for materials should be addressed to Zuankai Wang or Steven Wang.

Peer review information *Nature Communications* thanks Lihua Lyu, Chengyi Song, and the other, anonymous, reviewers for their contribution to the peer review of this work. A peer review file is available.